Usage Report for Fiscal Year 2023

Project Title:

Computational Studies of Muon Locations, Electronic Structures and Electron Transport in High T_c Superconductor, Organic, Organometallic, and Biological Systems

Name:

○Wan Nurfadhilah Zaharim (1,2), Dita Puspita Sari (2,3), Muhammad Redo Ramadhan (2,4), Irwan Ramli (2,5), Peter Greimel (2), Supparat Charoenphon (2,6), Phantip Jaikaew (2,7), Shukri Sulaiman (1) Isao Watanabe (2)

Laboratory at RIKEN:

(1) Universiti Sains Malaysia, Malaysia

(2) Nuclear Structure Research Group, RIKEN Nishina Center, Japan

(3) Shibaura Institute of Technology, Japan

(4) UPN Veteran, Yogyakarta, Indonesia

(5) Universitas Cokroaminoto Palopo, Indonesia

(6) Kasetsart University, Thailand

(7) Chiang Mai University, Thailand

1. Background and purpose of the project, relationship of the project with other projects

i Exploring various DFT functional to optimize $LiCoO_2$

It is known from previous studies, that the Li_xCoO_2 system vary their lattice parameter with the reduction of Li ions when battery-charging process are conducted. While experimental studies of this theme have been conducted in the past, clear evolution of the crystal structure from room temperature to very low temperature (< 10 K) have never been addressed in the past. Here density functional theory (DFT) calculation can be utilized to observe the optimized crystal structure at 0 K of $LiCoO_2$ system. Furthermore, DFT calculation can be combined with the muon spin resonance technique (DFT+μ) to provide accurate values of Li-ion diffusion coefficient which increase our understanding on the electrochemical performance of battery system.

However, it is not so easy to conduct DFT+μ for the Li_xCoO_2 system, as the chosen DFT functional needs to be determined carefully. Currently, there are 3 rungs of the most-utilized DFT functional known as: LDA (local density approximation), GGA (generalized gradient approximation), and metaGGA (GGA with the additional kinetic energy consideration). Those three functionals are mostly chosen due to its efficient computational cost compared to the very heavy hybrid-DFT calculations.

Based on those facts, four different functionals (LDA-PZ, GGA-PW91, GGA-PBE, metaGGA-SCAN) are chosen to compare the calculated lattice parameters with the known experimental lattice parameter at low temperatures. For simplicity, we call those functionals as PZ, PW91, PBE, and SCAN. From this calculation, we can obtain the best DFT functional to be utilized for the $LiCoO_2$ system. This will provide solid groundwork when continuing to the more advanced, DFT+μ calculation.

ii Electronic and magnetic properties in $Nd_2Ir_2O_7$

Nowadays, metal oxides play a significant role in many parts of chemistry, physics, and materials

science. Metal elements can form a large variety of oxide compounds. They can adopt many structural geometries with an electronic structure introducing metallic, semiconductor, or insulator characteristics. Metal oxides exhibit various functional properties, enormously depending on their crystal structure, morphology, composition, intrinsic defects, doping, etc., which determine the physical properties such as optical, electrical, and magnetic properties of the material. In this research, we aim to study the effects of point defects, including intrinsic and external impurities, on the physical properties of metal oxide compounds as follows ZnO and Nd2Ir2O7.

In general, the physical properties of a material can be obtained from quantum mechanical wavefunction by directly solving the Schrodinger equation in each system. The analytical solutions of the Schrödinger equation are obtainable only for simple systems. However, the systems that contain a large number of electrons, which are called the many-body systems, are not practical to be solved. Currently, density functional theory (DFT) and high-performance computers can simplify the Schrödinger equation of a many-electron system into a solvable problem by focusing on the electron density instead of the many-body wave function. The ground state energy, electron density, and related properties of ordinary matter can be computed efficiently when approximating the exchange-correlation energy as a function of the electron density. Thus, Jacob's ladder description refers to various levels of complicate and accuracy of approximations for the exchange-correlation energy as a functional of the electron density in DFT from the local density approximation (LDA) to generalized gradient approximations (GGA), meta-GGA, and hybrid functionals.

Over the years, The DFT approach has been prevalent for predicting various properties of materials, such as the crystal and electronic structure, optical properties, stability, etc., because it is reliable compared with experimental results. We divide the topic in this thesis into two main parts. The first part uses DFT calculation to study point defects and impurities in ZnO. And the second part uses DFT calculation to investigate the muon-stopping site in Nd2Ir2O7.

iii Organic conductor, magnets, λ-$(STF)_2FeCl_4$ and relative compounds (Dita)

(a) The organic superconductor λ-$(BETS)_2GaCl_4$ [BETS=$(CH)_2S_2Se_2C_6Se_2S_2(CH_2)_2$] is an unconventional superconductor. The so-called distorted nodal line was reported in the previous report from our μSR experiment, and we revealed from the DFT calculation the detail structure of the distorted Fermi surface in λ-$(BETS)_2GaCl_4$, owing to its lattice which is an anisotropic triangular alternating with squared lattice. When the Ga is replaced by Fe the metallic state undergoes insulating state instead of superconducting. This coincides with the antiferromagnetic (AF) transition. Moreover, when the magnetic field is applied parallel to the conducting plane, there is a compensation to the internal field and eventually superconductivity appears above 17 T. The AF ground state mechanism in this exotic field-induced superconductor is still in debate, since the driving force of is unclear, whether it is pi-electron of the large BETS molecule, or 3d-electron from the Fe element. Also, the AF transition is simultaneously occurred with the metal-insulator transition, making the discussion complicated. To understand the AF ground state, we studied the sister compound λ-$(STF)_2FeCl_4$ [STF=$(CH)_2S_4C_6Se_2S_2(CH_2)_2$, reducing the Se content in the large donor molecule. In λ-$(STF)_2FeCl_4$ there is no metal-insulator transition. We measured zero-field μ^+SR on λ-$(STF)_2FeCl_4$ and estimated the internal field. However, the DFT calculation is necessary to

(b) The hole-doped organic metal κ-$(ET)_4Hg_{3-\delta}Br_8$, δ=11% (κ-HgBr) and κ-$(ET)_4Hg_{3-\delta}Cl_8$, δ=22% (κ-HgCl), where ET=$(CH_2)_2S_8C_6S_8(CH_2)_2$, are exceptional carrier-doped metal among half-filled organics, beside ET dimers with spin-half (S=1/2)

tend to arrange triangular lattice. κ-HgBr is superconductor below 4.3 K while κ-HgCl transitions to the insulator at ambient pressure and becomes superconductor above 0.5 GPa. κ-HgBr shows non-Fermi liquid (NFL) behavior evidenced by linear temperature dependence of resistivity, $\sqrt{\rho(T)}$, and the ^{13}C-NMR measurement in the field of 9.4 T suggesting that the strong AF spin fluctuations contribute to the origin of NFL. The transverse field (TF) μ$^+$SR measurement in the field of 6 T further shows a deviation from the linearity of the susceptibility against the μ$^+$ Knight shift $\sqrt{K(\chi)}$, at temperatures below 50 K, unlike other κ-type FL organics.

We performed TF μ$^+$SR in κ-HgCl to understand the underlying correlation of the enhanced antiferromagnetic spin fluctuations, NFL, and superconductivity in these systems. The measurement has been done on the NuTime spectrometer at TRIUMF maintaining the experimental condition as that for κ-HgBr. We estimated the hyperfine coupling constant between muon and electron from the slope of the $\sqrt{K(\chi)}$ plot. The DFT calculation on κ-HgBr and κ-HgCl will be carried out to estimate the muon site and the hyperfine coupling constant.

iv Short Double Strand DNA molecule

Electron transport is essential for many vital biological processes, such as DNA UV damage repair, enzyme reactions, and energy storage and consumption. SR is an experimental method that can be utilized to investigate electron transport processes in DNA at the microscopic level. Muon hyperfine interactions, which are highly sensitive to changes in the electronic structure surrounding the muonium (Mu) trapping sites, can be used to investigate changes in the electron transport properties resulting from DNA damage. Establishing baseline data using DNA systems with known DNA sequences is therefore essential to systematically evaluate the impact of damage to DNA on electron behavior.

In an earlier study, the Mu hyperfine interactions at every potential Mu trapping site in four nucleobases, four nucleotides, four homogenous single-strand DNA oligomers and three homogenous 12mer single strand DNA were examined. For the 12mer single strand DNA, the results show that adding a sugar-phosphate group to the nucleic acid bases has a direct effect on the system's electronic structure. The geometry of cytosine, adenine, and thymine nucleobases were tested for distortion when Mu was added to the possible trapping sites. The optimized muoniated systems structure was examined to see if the presence of Mu caused the all the three bases ring to deviate from their planar shape.

Thus, in FY2023, double strand DNA with homogeneous nitrogenous bases was chosen as a model for this study. In this investigation, we performed DFT calculations to determine the geometry, electronic structure, and molecular properties, as well as Mu trapping sites, in ds(GC), ds(GC-CG), and ds(GC-CG-GC) base pair of guanine-cytosine double strand DNA molecules.

v Muon beamline simulation

In nature, muons come from the cosmic rays interacting with gas molecules in the earth's atmosphere. However, muons can be produced on earth by a particle accelerator. The μSR experiment requires low energy muon (surface muon) because it must stop at sample being studied. The low energy muon is the product of two-body pion decay. Pions are produced with sufficient numbers from collisions of high-energy protons (>300 MeV) with the nuclei of an intermediate light element target such as graphite or beryllium.

The surface muon serves as a valuable quantum beam in various scientific fields, including materials science and other disciplines. At the muon science facility, Japan Proton Accelerator Research Complex (J-PARC), there are two surface muon beamlines that are being used for actual experiments, S1 and S2. Our group plans to install a new muon beamline, S3. The

new S3 beamline is aimed to provide the strongest worldwide positron counting rate and highest quality of muon-spin resonance (μSR) time spectrum. As the first step, we conducted muon beam properties at the S-line entrance including the effect of leakage field from the H-line.

A beamline of muon beam basically consists of four main components: first, a decay section which is a superconducting solenoid magnet where the pions convert to muons by π-μ decay. Second, dipole magnet for bending the trajectories of muon beam. Third, quadrupole magnet for muon beam focusing. Fourth, DC separator or Wien filter for rotating muon spin angle and removing the muon beam contamination of electrons/positrons. In addition, septum magnets and kicker magnet is usually installed to inject the muon beam into each experimental station.

2. Specific usage status of the system and calculation method

i Exploring various DFT functional to optimize $LiCoO_2$

Vienna Ab initio Simulation Package (VASP) v.5.4.4 software is utilized to conduct DFT calculation for the unit-cell structure of $LiCoO_2$. The initial crystal structure is in the rhombohedral phase ($R\bar{3}m$) with the lattice parameters of $a = 2.8142$ Å and $c = 14.0435$ Å as shown in Figure 1, before fully-optimized (both ions and cell volume are relaxed) with the convergence criteria of 1×10^{-5}eV and 0.01 eV/Å for both energy-difference and force between atom respectively based on four different functionals as.

These convergence criteria have been proven to provide good accuracy and can be implemented on the DFT+μ calculation. No spin-polarized calculation is considered in the current project, due to the absent of magnetic ordering for $LiCoO_2$ based on the previous experimental studies. The Brillouin zone of this system is simulated by using the gamma-centered k-points arrangement of $13 \times 13 \times 3$ Here, we also consider the effect of different energy cutoff for the plane-wave basis set, where we set 520 eV and 600 eV along with the default value of 400 eV as implemented in VASP software. To standardize our method, we utilized 96 cores of HOKUSAI BWMPC for all calculations conducted within this study. This could provide good insight when designing larger supercell structure for modelling Li_xCoO_2 (x<1) in the future project.

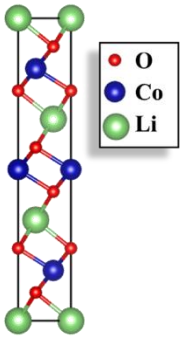

Figure 1. Initial crystal structure of LiCoO2

ii Electronic and magnetic properties in $ZnSb_2O_4$ and $Nd_2Ir_2O_7$

Our DFT calculations were employed within the Generalized Gradient Approximation Perdew-Wang91 (GGA-PW91), Meta-generalized gradient (Meta-GGA) and hybrid functionals (HSE) scheme, and the pseudopotential projector augmented wave (PAW) method for the electron–ion interactions as implemented in the Vienna ab initio simulation package (VASP). The Vienna Ab initio Simulation Package (VASP) is a computer program for atomic scale materials modeling, e.g. electronic structure calculations and quantum-mechanical molecular dynamics, from first principles. MATLAB is a high-performance language for technical computing that integrates computation, visualization, and programming in an easy-to-use environment. Wannier90 was also used in this project. It is an open-

source code for generating maximally localized Wannier functions and using them to compute advanced electronic materials with high efficiency and accuracy. It is proven that the HOKUSAI Great Wave supercomputer facility is crucial and extremely useful for our group research, particularly for large-scale calculations due to the results obtained from the calculations by using all the resource units.

iii Organic magnets, λ-$(STF)_2FeCl_4$ and relative compounds (Dita)

We discuss the positions of the two muon sites from the density functional theory (DFT) calculation performed within Kohn-Sham approach using the projector augmented-waves formalism in the VASP program. The exchange-correlation function generalized gradient approximation, GGA-PW91, was used. The ground-state charge densities were calculated by adopting the value of the crystal axis determined by the X-ray diffraction measurement, and by using the $6 \times 5 \times 2$ k-point sampling, ultrasoft pseudopotentials, and plane-wave densities.

iv Short Double Strand DNA molecule

Gaussian 16 was used for all computations. A hydrogen atom is utilized to simulate a Mu in muon site computation. Following Mu's introduction into the host system, further geometry optimization was done, allowing Mu and all atoms in the specific nitrogenous base where Mu was confined to relax to new locations. In Gaussian 16, the convergence conditions for the Self Consistent Field iteration and geometry optimization technique are set to the default settings. The converged electronic structures were then utilized to investigate the systems' characteristics and muon hyperfine interaction at the trapping location.

v Muon beamline simulation

The simulations were performed utilizing Geant4 and G4beamline. Both are particle tracking simulation programs, using the Monte Carlo method to sample interactions of particles in each step through matter. Physics models of the interactions are contained in the "physics list" providing different choices of electromagnetic and hadronic interactions. For primary particle energy lower than 5 GeV, QGSP-BERT is one of the recommended physics lists, which uses the quark-gluon string model and the Geant4 Bertini cascade model for the Hadronic process. For charged particles, standard electromagnetic physics is used, and the modeling of decays is also included. In the simulation, a 3 GeV proton beam is delivered to hit the muon target. By placing two virtual detectors with the same size as the target (radius = 168 mm), close to both sides of the surface of the target, we can calculate the proton transmission Furthermore, we provide information regarding the pion and muon yield from both sides of the target. Moreover, we studied at another position, the entrance of the S-line is located at 356 mm from the target with an angle of 45 degrees respecting the proton beam and the diameter of the aperture is 230 mm. To gather surface muons, quadrupole magnets are employed illustrated in Figure 2. as pink tubes. As mentioned above, the H-line is located next to the S-line with 75 degrees regarding the center of the S-line, the leakage magnetic field from the capture solenoid magnet, HS1 at H-line, is concerned and included in the simulation.

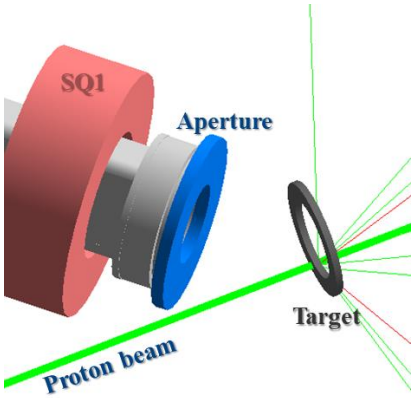

Figure 2. Simulation set up in G4beamline.

3. Result

i Exploring various DFT functional to optimize $LiCoO_2$

All calculated results based on the current study are tabulated on Table 1. Based on the known experimental lattice parameter values of $a = 2.8120$ Å and $c = 14.0303$ Å at 300 K, only SCAN functional can provide least error albeit with lower values. The lower values given by SCAN parameter is due to the fact that the DFT method provide the results at 0 K. This fact is supported by the known experimental study where the lattice parameter values of $LiCoO_2$ are reduced when temperature is decreased. For instance, the value of a is reduced to ~2.8050 Å at the temperature of 100 K (from 2.8050 Å at 300 K). Similar trend is also observed for the c lattice parameter, which suggest that the **SCAN functional is the best choice** for the $LiCoO_2$ system. Considering that $LiCoO_2$ is a non-magnetic system, the on-site Coulomb potential (U) is not required, thus detailed calculation can be carried out without including U factors on future calculation.

To prepare our future DFT+μ project on the supercell structure of $LiCoO_2$ system, we provide the calculation time and the memory usage for each calculation conducted within this study. Our results, show that the larger energy cutoff that we used, the more computational memory is required. As the calculated lattice parameter values between 520 eV and 600 eV do not vary so much for all utilized DFT functional, it might be more efficient for the future supercell study to only consider the 520 eV as the energy cut off, as the DFT calculation on the supercell structure requires a very large amount of memory to store any information from the calculations grid.

Tabel 1. Calculated lattice parameter, time and memory usage for $LiCoO_2$

	PZ	PW91	PBE	SCAN
	400 eV			
a (Å)	2.7741	2.8253	2.8226	2.7884
c (Å)	13.4902	13.7853	13.7863	13.7605
Time (s)	1908	390	618	1135
Memory (Mb)	228	220	228	232
	520 eV			
a (Å)	2.7907	2.8556	2.8513	2.8075
c (Å)	13.6016	14.0117	14.0018	13.9565
Time (s)	1406	586	817	595
Memory (Mb)	247	236	240	243
	600 eV			
a (Å)	2.7908	2.8546	2.8503	2.8086
c (Å)	13.5978	13.9974	13.9892	13.9546
Time (s)	1796	464	770	771
Memory (Mb)	246	242	242	249

ii Electronic and magnetic properties in $ZnSb_2O_4$ and $Nd_2Ir_2O_7$

Our aim in the present work is to investigate the likelihood of the formation of native point defects and the electronic properties of these defects using the screened hybrid-functional proposed by Heyd, Scuseria, and Ernzerhof (HSE). First, we determine the bulk properties of $ZnSb_2O_4$, such as lattice parameters, electronic structure, bang-edge position, formation enthalpy, and equilibrium growth chemical potential diagram.

We then explore the thermodynamic stability of all

possible native defects in $ZnSb_2O_4$, including zinc, antimony, and oxygen vacancies (V_{Zn}, V_{Sb}, and V_O), the interstitials (Zn_i, Sb_i, and O_i) and the antisites (Sb_{Zn}, Zn_{Sb}, Sb_O, Zn_O, O_{Sb} and O_{Zn}) through the formation energies calculated under representative growth conditions. The local atomic structure and electrical properties of these defects are examined. The results show that carrier compensation due to the native defects is likely to make as-grown $ZnSb_2O_4$ semi-insulating. In addition, we investigate the energetics and electronic properties of cation and anion impurities such as Al, Ga, In, and F, which are expected to act as donors. We will discuss how these impurities affect the Fermi level and, therefore, the possibility of n-type doping in $ZnSb_2O_4$.

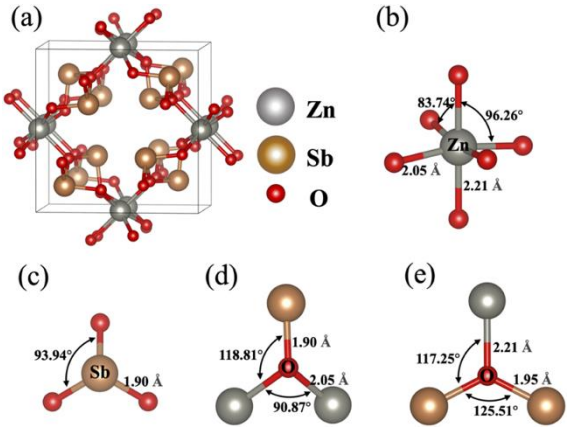

Figure 3: (a) An illustration of $ZnSb_2O_4$ primitive cell containing 28 atoms and its local atomic structure. (b) Zn, (C) Sb, (c) type-I O, and type-II O atoms. The calculated equilibrium Zn–O and Sb–O bond lengths and angles are also listed.

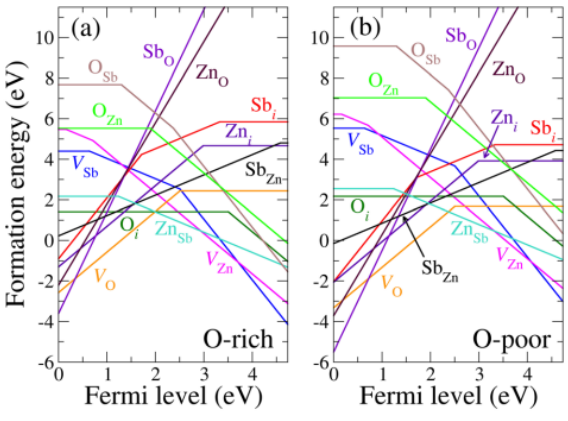

Figure 4: Formation energies as a function of Fermi level position for native point defects in $ZnSb_2O_4$. The results are shown for (a) the O-rich limit and (b) the O-poor limit. The zero of the Fermi level corresponds to the VBM and CBM. Only segments corresponding to the lowest energy charge states are shown. The slope of each segment indicates the charge state. Kinks in the lines for the same defect indicate the thermodynamic transition levels.

To utilize $ZnSb_2O_4$ in practical applications such as pseudocapacitive devices, enhancing charge carriers is often required. This material may be feasible for n-type doping based on the relatively low position of the conduction band edge. Here, we investigate the possibility of doping with impurities expected to act as electron donors, including Al, Ga, In, and F. The likelihood of these impurities was investigated through the calculated formation energies as a function of the Fermi level. For the metal impurities (Al, Ga, and In), we consider three possible configurations, including the metal atom substituted for Zn (Al_{Zn}, Ga_{Zn}, and In_{Zn}), metal substituted for Sb (Al_{Sb}, Ga_{Sb}, and In_{Sb}), and interstitials (Al_i, Ga_i, and In_i). For F, only two configurations, F substituted for O (F_O), and F interstitial (F_i), were considered; F substituted for Zn, and Sb would cause very high formation energies due to large differences in their ionic radii.

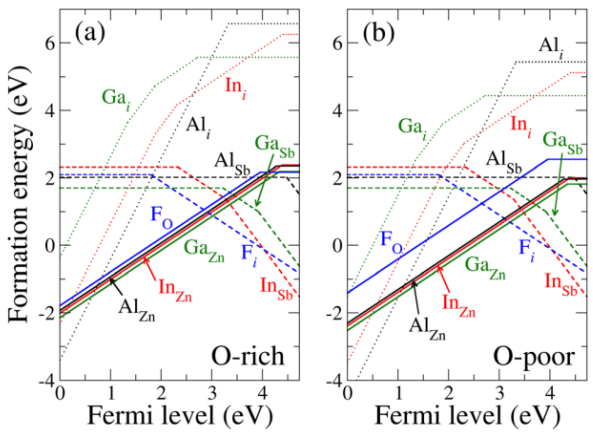

Figure 5: Formation energy as a function of the Fermi level of Al, In, Ga, and F impurities in $ZnSb_2O_4$. The results are shown for (a) the O-rich limit and (b) the

O-poor limit. The zero of the Fermi level corresponds to the VBM and CBM. Only segments corresponding to the lowest energy charge states are shown. The slope of each segment indicates the charge state. Kinks in the lines for the same defect indicate the thermodynamic transition level.

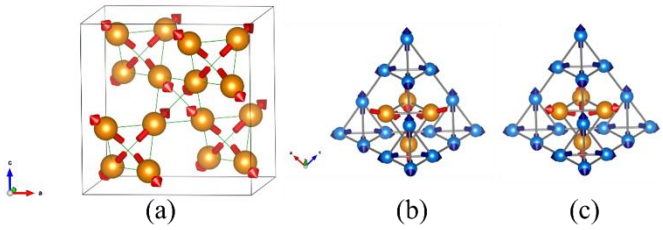

Figure 6: (a) All-in all-out magnetic structure. The filled circles represent Nd3+ ions, and the arrows represent the Nd moments. Two domain spin structures for the all-in–all-out state (b) Relation between magnetic moments (blue thin arrows) of Ir4+ ions (blue small balls) and mag-netic moments (red thick arrows) of Nd3+ ions (red large balls). Both the Ir and the Nd moments form the all-in allout structures. Alternative directions of Nd moments in the case of a ferromagnetic Nd-Ir interaction. (c) Antiferromagnetic Nd-Ir interaction

The GGA calculation, with separate adjustments to the U_d of Ir and U_f of Nd, effectively rectifies the lattice parameter and magnetic moment values for Ir and Nd. However, despite these adjustments, the band gap remains closed. The U_d value is around 5 eV on empty d-orbitals of Ir, and the U_d value is approximately 5-8 eV on empty f-orbitals of Nd. It was also shown that it was necessary to open a band gap of $Nd_2Ir_2O_7$ from metal to insulator, which is consistent with the experimental value. We have adopted U_d = 3 eV and varying U_f of Nd from 5 to 8 eV to describe and discuss the electronic structure, elastic constants, and mechanical properties of $Nd_2Ir_2O_7$ shown and compared with previous experimental studies. The cell lattice of the $Nd_2Ir_2O_7$ cubic cell ranges from 10.3841 to 10.4066 Angstrom as a function of U (Table 3), which agrees with the experimental value (10.4040 ˚ A). Indeed, we have a maximum percentage error of 1.54 for U_d and U_f = 5 and 8 eV, respectively. We illustrate the evolution of the density of states with U_d of Ir and U_f of Nd for $Nd_2Ir_2O_7$. The most distinct feature we observe apart from the continuous try to open the band gap by fixing U_d = 5 eV with increasing U_f of Nd from 5 to 8 eV. The range of energies over which electronic states are spread out is narrower. In this system, the GGA+U valence bandwidth decreases by 1 eV over a U range from 5 to 8 eV. The transition metal 5d electrons hybridize strongly with the 4f, and the oxygen 2p states and their relative energetic position determine the degree of hybridization and the width of the valence band. As the occupied 5d states move toward lower energy, the top of the valence band develops more O 2p character with increasing U. move toward lower energy, the top of the valence band develops more O 2p character with increasing U correction may not be sufficient to turn metal into an insulator. The calculation magnetic moment of Ir for insulator $Nd_2Ir_2O_7$ is 0.31 μ_B. The best agreement with the experimental value (0.5 μB) is found for U_d = 5 eV and U_f = 5 eV. However, for the range of U_f = [5–8] eV, the percentage error is relatively small, at less than 5.5, in good agreement with previous reports. We note an increase in the magnetic moment of the Nd atom for cubic $Nd_2Ir_2O_7$ is constant around 2.98-3.00 μ_B, which is higher than the experimental value (2.3 μ_B).

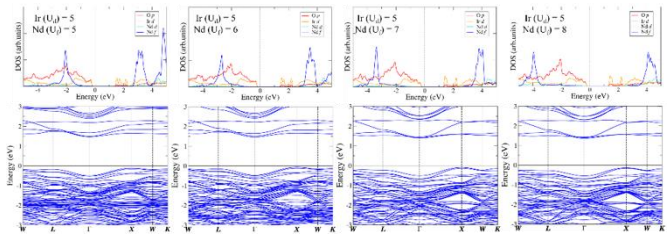

Figure 7: Obtain the density of state and band structure of $Nd_2Ir_2O_7$ within GGA+U. The fermi energies are set to zero.

The results from this current work have been presented at the international conference as listed in

the List of Publication section of this report.

iii Organic magnets, λ-$(STF)_2FeCl_4$ and relative compounds (Dita)

Here we would like to report two results on the organic magnet λ-$(STF)_2FeCl_4$ and organic superconductor κ-$(ET)_4Hg_{2.89}Br_8$.

(a) From μSR experiment we found two kinds of development of internal field, one shows a large internal field and the other is 10 times smaller, shown in Fig. 6a. We reported the muon site calculation on λ-$(STF)_2FeCl_4$. Two possible muon sites were found, close to Fe and close to H atom. However, at this stage we could not distinguish which site related to the large or small internal field.

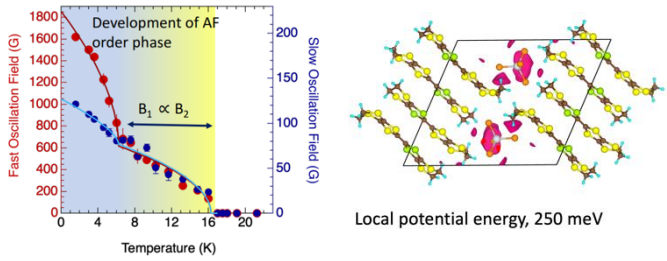

Figure 6a. (left) The development of internal field measured by μSR experiment. Two internal field were estimated as in the order of 2000 G and 120 G. (right) The possible muon-site, which is located close to Fe atom.

(b) The muon site on κ-$(ET)_4Hg_{2.89}Br_8$ is estimated to be in between ET dimer, not so close to the center of the dimer itself. It can support the estimation of the hyperfine coupling constant from the muon Knight shift experiments on κ-$(ET)_4Hg_{2.89}Br_8$ and κ-$(ET)_4Cl_{2.78}Cl_8$ which is only in the order of 200 Oe/μ_B.

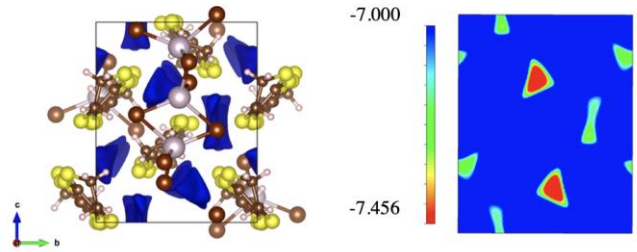

Figure 6b. Refined electronic potential calculation

iv Short Double Strand DNA molecule

The results reported here were based on our published data on the double strand DNA molecules. The initial geometry of ds(GC), ds(GC-CG), and ds(GC-CG-GC) are in planar shape. After the optimization process, all of the molecules maintain their planar characteristics. Figure 8 shows the optimized structure of all the three molecules.

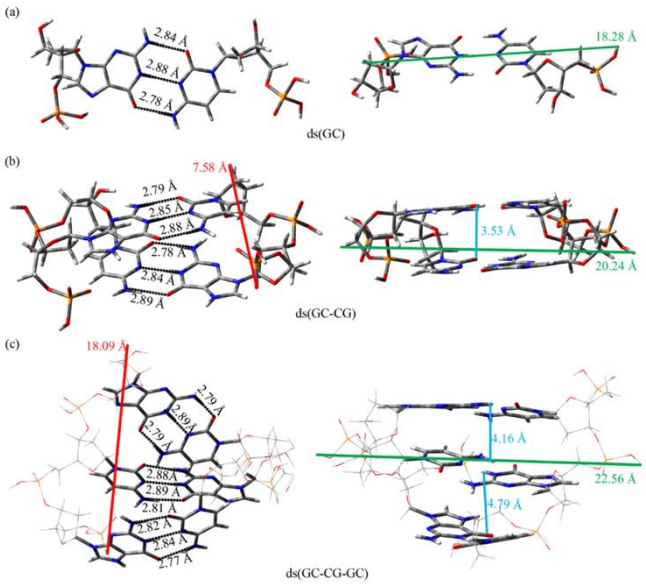

Figure 8: Shapes and dimensions of (a) ds(GC), (b) ds(GC-CG), and (c) ds(GC-CG-GC). On the left side of the figure, the red lines represent the lengths while the dotted lines represent the distances of O6–N4, N1–N3, and N2–O2. The green and blue lines on the right side of the figure represent the widths and distances between base stacking, respectively.

The total number of possible Mu trapping sites in ds(GC), ds(GC-CG), and ds(GC-CG-GC) are 14, 28, and 42, correspondingly. Table 2, and 3 presents the relative energies sorted in ascending order and other calculated data for ds(GC), and ds(GC-CG). For ds(GC), C8-G-B1 has the lowest total energy, which is 79,275.880 eV. The relative energies of the 14 sites lie in the range of 2.465 eV. The Mu site with the highest energy is O6-G-B1. The calculated muon HFCC at C8-G-B1 in ds(GC) is 378.7 MHz. The second most stable Mu site is N3-C-B1 with the

relative energy of 0.367 eV and muon HFCC of -23.7 MHz. In ds(GC-CG), C8-G-B2 is the most energetically stable Mu site followed by C8-G-B1, the latter being 0.002 eV higher in energy. The calculated muon HFCC at the two sites are 364.9 and 363.5 MHz respectively, about 6% lower than the value in ds(GC). C5-C-B2 and C5-C-B1 in the cytosine bases are the third and fourth possible Mu sites with very similar relative energies of 0.530 and 0.532 eV. At C5-C-B2 and C5-C-B1, the calculated muon HFCC are 89.8 and 88.4 MHz. C6-C-B1 and C6-C-B2 are ranked sixth and seventh in the ascending order of relative energy, 0.558 eV higher than C8-G-B1. The corresponding calculated values of muon HFCC are 523.0 and 534.7 MHz. C6 and C5 are more favorable sites than N3 of cytosine base in the ds(GC-CG) system, which is opposite to the case of ds(GC).

Table 2: Relative energy of the 14 sites in ds(GC) arranged in ascending order, as well as other calculated data.

Molecules	Relative energy (eV)	HFCC (MHz)	Estimated ALC-μSR resonance (T)
C8-G-B1	0.000	378.7	1.4
N3-C-B1	0.367	-23.7	-0.1
N7-G-B1	0.753	35.3	0.1
C5-C-B1	0.787	148.3	0.5
C6-C-B1	0.795	510.0	1.9
C6-G-B1	1.061	174.8	0.6
C5-G-B1	1.308	611.0	2.2
C4-G-B1	1.344	528.8	1.9
O2-C-B1	1.475	-2.2	0.0
N3-G-B1	1.586	102.6	0.4
C2-G-B1	1.662	367.1	1.3
C2-C-B1	2.288	-1.0	0.0
C4-C-B1	2.340	1809.2	6.6
O6-G-B1	2.465	-25.2	-0.1

Table 3: Relative energy of the 28 sites in ds(GC) arranged in ascending order, as well as other calculated data.

Molecules	Relative energy (eV)	HFCC (MHz)	Estimated ALC-μSR resonance (T)
C8-G-B2	0.000	363.5	1.3
C8-G-B1	0.002	364.9	1.3
C5-C-B2	0.530	89.8	0.3
C5-C-B1	0.532	88.4	0.3
C6-C-B1	0.558	523.0	1.9
C6-C-B2	0.558	524.7	1.9
N3-C-B2	0.789	-21.3	-0.1
N3-C-B1	0.804	-21.7	-0.1
C5-G-B1	0.946	534.6	1.9
C5-G-B2	0.946	533.4	1.9
C4-G-B2	1.191	450.1	1.6
N3-G-B2	1.217	13.0	0.0
C4 -G-B1	1.222	483.5	1.8
O6-G-B2	1.226	-14.7	-0.1
N7-G-B2	1.253	161.6	0.6
N7-G-B1	1.268	161.1	0.6
N3-G-B1	1.269	10.2	0.0
O6-G-B1	1.398	280.6	1.0
O2-C-B2	1.771	461.0	1.7
C2-G-B2	1.772	348.0	1.3
C2-G-B1	1.798	545.7	2.0
O2-C-B1	2.015	-2.4	0.0
C6-G-B1	2.077	-11.6	0.0
C6-G-B2	2.079	-13.8	-0.1
C2-C-B2	2.118	1827.6	6.6
C4-C-B2	2.141	1741.4	6.3
C4-C-B1	2.145	1758.6	6.4
C2-C-B1	2.288	-23.6	-0.1

To visualize the relative positions of Mu sites in ds(GC-CG-GC) with respect to energy and HFCC, we plot the data using a scatter plot as shown in Figure 9. We have excluded the ten highest sites from the scatter plot because their relative energies are more than 2 eV. As in the case of ds(GC) and ds(GC-CG), all three C8 Mu sites in ds(GC-CG-GC) have the lowest energies. Among these three sites, the most stable Mu site is C8-G-B1, followed by C8-G-B3 and C8-G-B2. In contrast to ds(GC-CG) where the energies of the two C8 sites differ by only 0.002 eV, the differences in the energies of the three C8 sites in ds(GC-CG-GC) are more pronounced. The relative energy of C8-G-B3 which is the second most stable site is 0.184 eV and the next site, C8-G-B2 has even higher relative energy of 0.293 eV. The muon HFCC for these three lowest energy sites are 355.2, 348.5, and 409.3 MHz, where the range between the lowest and the highest HFCC is 60.8 MHz.

After the three lowest energy C8 sites in guanine

bases in ds(GC-CG-GC), the next four sites are C6-C-B3, C6-C-B2, C5-C-B2, and C5-C-B3. Their relative energies are more than 0.454 eV. The calculated muon HFCC for C6-C-B3 and C6-C-B2 are 521.4 and 565.4 MHz respectively. There is also a significant increase in going from C6 to C5 of cytosine base.

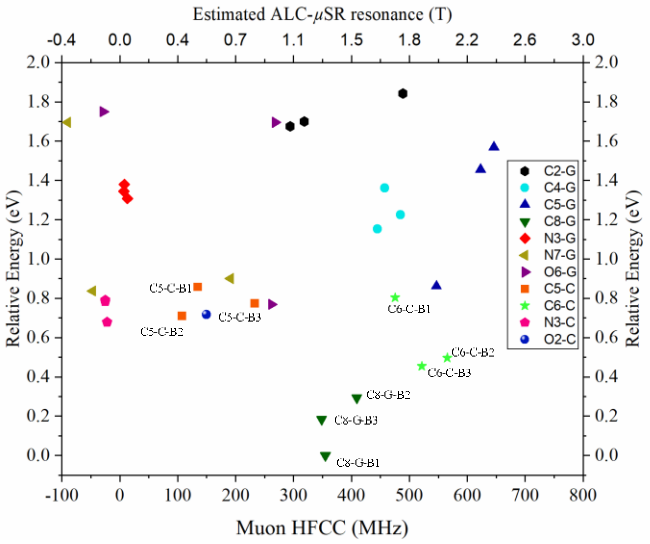

Figure 9: Scatter plot of relative energy and Mu HFCC of ds(GC-CG-GC) Mu trapping sites.

iv Muon beamline simulation

The first section is the area of the muon target to study muon production, the scattered distribution of particles around the muon target area, we can calculate the proton transmission which is approximately 95%. For the pion yield, and muon yield were presented in Table 4.

Table 4: The pion and muon yield at both sides of the target surface.

Particle types	Counted per primary protons	
	Backward	Forward
Pion	3.60×10^{-3}	2.21×10^{-2}
Muon	2.78×10^{-5}	3.82×10^{-5}
Surface muon[1]	1.40×10^{-6}	1.50×10^{-6}

[1]Muons have kinetic energy in the range 3.70 - 4.00 MeV

In the second section, the muon beam properties at the S-line entrance are described including the effect of leakage field from the H-line. We have computed the fraction of surface muons per primary proton, yielding values of 9.83×10^{-8} and 9.04×10^{-8} for the scenarios without and with a leakage field, respectively. The beam loss is approximately 8% when the leakage field is considered. The emittance and the Courant-Snyder parameters have been calculated and are presented in Table 5.

Table 5: Muon beam properties at the entrance of S-line.

Particle types	Horizontal (x)		Vertical (y)	
	without	with	without	with
Emittance (mm mrad)	4.84×10^{3}	4.69×10^{3}	4.57×10^{3}	5.63×10^{3}
β	7.94×10^{-1}	8.27×10^{-1}	8.54×10^{-1}	6.48×10^{-1}
α	-1.88×10^{-3}	-1.99×10^{-3}	-2.06×10^{-3}	-1.42×10^{-3}

4. Conclusion

i Exploring various DFT functional to optimize $LiCoO_2$

Based on this study, we confirm that the best DFT functional for $LiCoO_2$ system is metaGGA-SCAN functional. From the memory usage perspective, we determine that both 520 and 600 eV are good enough to obtain converged values of lattice parameter. However, the memory usage is increased slightly which can affect the calculation's efficiency when supercell structure is considered.

ii Electronic and magnetic properties in $ZnSb_2O_4$ and $Nd_2Ir_2O_7$

We find that the HF fraction of 48% yields the calculated band gap and lattice parameters in good agreement with the experimental values. Our calculations for the energetics of the intrinsic point defects indicate that there are no shallow donor and shallow acceptor defects with low formation energies. The oxygen vacancy VO has the lowest formation energy among the donor-type defects under the O-rich and O-poor conditions. However, it acts as a very deep acceptor, unlikely to provide free electron carriers to the conduction band. Moreover, electron carriers are likely to be compensated by the formation of V_{Zn} and Zn_{Sb}, which behave as dominant acceptors.

Our analysis of the charge neutrality conditions estimates that the Fermi level of undoped $ZnSb_2O_4$ would be pinned in a range that is 2.39 eV to 2.80 eV above the VBM for the O-rich to O-poor growth conditions, respectively, suggesting that this material is semi insulating. We further investigate the possibility of enhancing free electron carriers by doping with Al, Ga, In, and F impurities, finding that Al_{Zn}, Ga_{Zn}, In_{Zn}, and F_O are single donors. Although Ga_{Zn} is the most viable donor impurity due to its lowest formation energy among other donor impurities, its concentration is reasonably low for the n-type conditions. Moreover, Ga_{Zn} would be compensated by Ga_{Sb}, which acts as an acceptor, thereby inhibiting high electron carrier concentration. The other donors Al_{Zn}, In_{Zn}, and F_O, also suffer from low solubility and self-compensation. The maximum pinned Fermi level of 3.52 above the VBM is attained in Ga-doped $ZnSb_2O_4$ under the O-poor conditions, resulting in a very low carrier concentration, which is insufficient for an effectiven-type semiconductor.

The electronic structures and magnetic properties of $Nd_2Ir_2O_7$ have been investigated using GGA + U scheme and relativistic spin orbit coupling (SOC). The effects of effective U values on the structural and electronic properties of pyrochlores have been studied. It is shown that for strongly correlated systems and necessary to cor-rect the intraband Coulomb interaction by the Hubbard U parameter. We suggest that the electronic structure can be reasonably described with U_{eff} of 5-6 eV for Nd 4f orbital and U_{eff} 5 eV for Ir 5d orbital show in DOS distribution. The DOS distributions of $Nd_2Ir_2O_7$ show that Nd 4f electrons hybridize significantly with Ir 5d orbitals in the valence region. The magnetic structure of this system can be described by the all in all out type of model for Nd moments with a magnitude of about 2.98 μB and Ir magnetic moment about 0.3-0.4 μ_B.We observe apart from the continuous try to open the band gap from metal to insulator, setting U_d of Ir and U_f of Nd are 5 and 5 eV, the estimated gap of $Nd_2Ir_2O_7$ shows 1.50 eV, the lattice parameter is 10.3841 close to the experimental value. Our results provide to support previous and future practicals.

iii Organic magnets, λ-$(STF)_2FeCl_4$ and relative compounds (Dita)

(a) The muon site on λ-$(STF)_2FeCl_4$ is estimated to be at 2 positions, which are close to Fe, close to H atom. The dipole field calculation on the muon at this stage could not distinguish which muon site that is related to the large or small internal field, estimated from the μSR experiment.

(b) The muon site on κ-$(ET)_4Hg_{2.89}Br_8$ is estimated to be in between ET dimer, not so close to the center of the dimer itself. It can support the estimation of the hyperfine coupling constant from the muon Knight shift experiments on κ-$(ET)_4Hg_{2.89}Br_8$ and κ-$(ET)_4Cl_{2.78}Cl_8$ which is only in the order of 200 Oe/μ_B.

iv Short Double Strand DNA molecule

DFT cluster method was successfully employed to investigate the geometry, electronic structures, and molecular properties, as well as Mu trapping sites, in ds(GC), ds(GC-CG), and ds(GC-CG-GC). The possible muon trapping sites were analyzed from the relative energy and muon HFCC values. For all the three molecules, C8 site is the most probable Mu trapping sites.

v Muon beamline simulation

95% of the proton beam passes through the muon target and collides with the neutron target. The momentum distribution of surface muon between backward and forward is nearly symmetrical. Surface muon beam position distribution on the horizontal is asymmetrical because of the location of the S-line. Because of the leakage field, the beam loss is approximately 8%, and emittance in the vertical axis

increases. So transverse beam size is larger, and the beam is more divergent.

5. Schedule and prospect for the future

i DFT+μ calculation on $LiCoO_2$ and $LiFePO_4$ to estimate diffusion coefficient

For the next project (Jan-Mar) we will proceed to the calculation of DFT+μ of $LiCoO_2$ based on the DFT SCAN functional. Our initial calculation shows that there are two minimum potentials for this system, suggesting that two possibilities for muon to be implanted in. Based on those, we will clarify the perturbation effect caused by the implanted muon inside the $LiCoO_2$ system. Furthermore, zero-point vibration motion (ZPVM) of muon will also be considered by mapping the muon probability distribution map based on the electrostatic potential data.

To obtain accurate results on the muon's perturbation effect. Supercell structure of $LiCoO_2$ with the arrangement of $2 \times 2 \times 1$ is required at the minimum. We will also try to expand the supercell structure to the arrangement of $4 \times 4 \times 1$ to reduce the possible spurious interaction caused by the implanted muon.

For the next part of our project, we will also test our method on LiFePO4 system (LFP). Key difference on this system compared to the previous system is the LFP considered to be magnetic. Similar with previous project, first we determine best functional to optimize the LFP system. As LFP considered to be magnetic, the on-site Coulomb potential need to be carefully considered. Here we only consider GGA and meta-GGA functional as the previous results show that LDA functional give largest error on the lattice parameter estimation of $LiCoO_2$. After we obtain the best functional, we can estimate muon hopping rate and separate its contribution to the fluctuation rate of the muon by looking into the ZPVM of the muon. By applying this method, we can get a reliable results of diffusion coefficient of Li-ion and contribute to the future development of battery materials

ii Electronic and magnetic properties in $ZnSb_2O_4$ and $Nd_2Ir_2O_7$

Next step, the GGA+U was carried out, including the muon, to reproduce the μSR results. We estimate the initial position of muon injection in $Nd_2Ir_2O_7$ obtained from the electrostatic potential. We will compare the result of calculation the GGA+U, meta-GGA and calculation internal field of possible muon position in $Nd_2Ir_2O_7$

iii Organic magnets, λ-$(STF)_2FeCl_4$ and relative compounds (Dita)

In the next step, we need to assume a magnetic structure in λ-$(STF)_2FeCl_4$ and re-calculate the muon site estimation. Meanwhile, the GGA calculation on κ-$(ET)_4Hg_{2.89}Br_8$ will be continued. The calculation in the sister compound κ-$(ET)_4Hg_{2.78}Cl_8$ will be planned to estimate muon-site, to obtain band structure and Fermi surface.

iv Short Double Strand DNA molecule

The optimized structure and the details information on the Mu trapping sites in ds(GC), ds(GC-CG), and ds(GC-CG-GC) have been obtained and published. Thus, the next fiscal year, we would like to obtain the electronic structure of short methylated double strand DNA molecules (me-dsGC, me-dsGC-CG, and me-dsGC-CG-GC) and their associate muon hyperfine coupling constant.

iv Muon beamline simulation

The simulation results will be applied for a beam dynamic calculation to design a new S by using beam optic calculation such as TRANSPORT and to simply optimize the magnetic elements in the beamline and then using the optimal data for G4beamline.

6. If no job was executed, specify the reason.

Usage Report for Fiscal Year 2023

Fiscal Year 2023 List of Publications Resulting from the Use of the supercomputer

[Paper accepted by a journal]

1. Mohd Tajudin, S. S., Zaharim, W. N., Sulaiman, S., Ahmad, S. N., Hasan Baseri, D. F., Ang, L. S., Risdiana, Safriani, L., & Watanabe, I. (2023). Functional Effect in Density Functional Theory Calculation of $Au_{23}(SR)_{16}$ Nanocluster. *Journal of Metastable and Nanocrystalline Materials* (Vol. 37, pp. 65-70). Trans Tech Publications Ltd.

2. Charoenphon, S., Tubtimtae, A., Watanabe, I., Jungthawan, S., Jiraroj, T., Boonchun, A., & Reunchan, P. (2023). The role of native point defects and donor impurities in the electrical properties of $ZnSb_2O_4$: a hybrid density-functional study. *Physical Chemistry Chemical Physics*, 25(28), 19116-19125.

[Conference Proceedings]

[Oral presentation]

1. Zaharim, W. N (March, 2023). DFT Studies on Electronic Structure of DNA. Invited speaker at *8th URICAS Conference, 2023 RIKEN Symposium*.

2. Zaharim, W. N (September, 2023). Density Functional Theory Investigation on the Electronic Structure and Muon Hyperfine Interaction in Isolated Guanine. Oral presentation at *The 11th ICMR Conference 2018*.

3. Zaharim, W. N (October, 2023). DFT Studies On Muon Hyperfine Interactions in Organic Materials. Seminar at *Workshop on Development of Organics and Biomass-based Materials and their Potential Applications.*

4. Zaharim, W. N (November, 2023). DFT Studies On Muon Hyperfine Interactions in DNA. Invited talk at *The 3rd International Symposium on Physics and Applications 2023.*

5. Sari, D. P, (September 2023). μSR study on the Spin Dynamics of κ-$(ET)_4Hg_{2.78}Cl_8$. *The Physical Society of Japan 2023 (78th) Autumn Meeting, 19aA200-8, Tohoku University, Japan.*

6. Sari, D. P, (September 2023). Organic Superconductivity Nearby Quantum Criticality of a Magnetic Frustration. Invited talk at *Muon User Meeting, Queens College, Oxford University, United Kingdom.*

[Poster presentation]

1. Jamaludin. A, Zaharim, W.N., Sulaiman, S., Rozak, H., Watanabe, I. (March, 2023). Density Functional Theory Investigation of Muon Hyperfine Interaction in Guanine-Cytosine Double-Strand DNA and Methylated Guanine-Cytosine Double-Strand DNA, *Poster presentation at 8th USM-RIKEN Interdisciplinary Collaboration on Advanced Sciences.* Institute for Research at Molecular Medicine, Universiti Sains Malaysia, Malaysia.

2. Charoenphon, S., Widyaiswari, U. Reunchan, P., Watanabe, I., (August, 2023) First-principles calculations of electronic and magnetic properties in Nd2B2O7 (B = Ru, Ir, Pt) by using GGA+U functional, *Poster presentation at RIKEN Summer School 2023*. Wako, Japan.

3. Charoenphon, S., Widyaiswari, U. Reunchan, P., Watanabe, I., (October, 2023). First-principles calculations of electronic and magnetic properties in Nd2Ir2O7 pyrochlore by using GGA+U functional, *Poster presentation at Computational Approaches to Quantum Many-Body Systems*. Saitama, Japan.

4. Zaharim, W.N., Sulaiman, S., Jamaludin. A, Rozak, H., Watanabe, I., (November, 2023). Density Functional Theory Investigation of the Electronic Structure and Muon Hyperfine Interaction in Isolated Adenine and Thymine. *Poster presentation at International Conference on Hyperfine Interactions and their Applications*.

5. Charoenphon, S., Widyaiswari, U. Reunchan, P., Watanabe, I., (November, 2023). First-principles calculations of electronic and magnetic properties in Nd2Ir2O7 pyrochlore by using GGA+U functional, Poster presentation at the International Conference on *Hyperfine Interactions and their Applications (HYPERFINE2023).* Nara, Japan.

6. Jaikaew, P., Rimjaem, S., Thongbai, C., Adachi, T., Shimomura, K., Koda, A., Watanabe, I., (November, 2023). Surface muon production at J-PARC muon facility. *Poster presentation at the International Conference on Hyperfine Interactions and their Applications* (HYPERFINE2023). Nara, Japan.

7. Dita P. Sari, Y. Cai, U. Widyaiswari, A. E. Putri, E. Yamada, Y. Someya, A. Koda, Y. Ishii, F. L. Pratt, I. Watanabe, K. M. Kojima, and H. Taniguchi (September 2023). μSR study on the Hole-doped Organic Metals κ-$(ET)_4Hg_{2.89}Br_8$ and κ-$(ET)_4Hg_{2.78}Cl_8$: Superconductivity Nearby Quantum Spin Liquid States*. International Long-term Workshop of Quantum Information, Quantum Matter, Quantum Gravity, Workshop number YITP-T-23-01.* Kyoto, Japan.

8. Dita P. Sari, Y. Cai, K. Kojima, I. Watanabe, H. Taniguchi, Y. Ishii, μ^+SR Knight Shift of the Hole-doped organic Metal κ-$(ET)_4Hg_{2.78}Cl_8$, *International Conference on Hyperfine Interactions and their Applications (HYPERFINE2023).* Nara, Japan.

9. Dita P. Sari, Y. Cai, U. Widyaiswari, A. E. Putri, E. Yamada, Y. Someya, A. Koda, Y. Ishii, F. L. Pratt, I. Watanabe, K. M. Kojima, and H. Taniguchi (November 2023). μSR study on the Hole-doped Organic Metals: Superconductivity Nearby Quantum Spin Liquid States. *International Conference on Machine Learning Physics.* Kyoto, Japan.

[Others (Book, Press release, etc.)]